AGU PUBLICATIONS

JGR

Journal of Geophysical Research: Oceans

RESEARCH ARTICLE

10.1002/2016JC012491

The importance of lateral variability on exchange across the inner shelf south of Martha's Vineyard, MA

A. R. Kirincich[1] and **S. J. Lentz**[1]

[1]Department of Physical Oceanography, Woods Hole Oceanographic Institution, Woods Hole, Massachusetts, USA

Abstract This study examines the spatial variability of transport within the inner-shelf south of Martha's Vineyard Massachusetts, its time and space dependence, and its importance to the total volume exchanged between the nearshore and the coastal ocean. The exchange of water across the inner shelf is often considered to be driven primarily by wind forcing, yet the effects of small-scale O(1–10 km) variability on the total exchange have not been well quantified. Using a combination of high-resolution HF radar-based surface currents and a dense array of moorings to document the lateral variability of across-shelf exchange, the cumulative wind-driven across-shelf transport over the summer stratified period was less than the volume of the inner-shelf onshore of the 25 m isobath. Along-shelf variations in the wind-driven exchange were as large as the spatial mean of the wind-driven exchange. A spatially varying time-averaged circulation caused by tidal rectification resulted in across-shelf exchange larger in magnitude than, and independent of, the integrated wind-forced exchange. Coherent submesoscale eddies also occurred frequently within the domain due to flow-topography effects onshore and horizontal density gradients offshore, generally with lifespans shorter than 10 h, diameters smaller than 6 km, and vertical depths shallower than 10 m. The across-shelf volume transport due to eddies, estimated by seeding particles within the surface current fields, was more than half the wind-driven depth-dependent exchange. Thus, accounting for the potential coherent along-shelf variability present over the inner shelf can significantly increase estimates of the across-shelf transfer of water masses and particles.

Key Points:
- The magnitude of the wind-driven surface transport across the inner shelf varied up to 50% over a 15 km along-shelf distance
- Coherent submesoscale eddies were responsible for volume exchange equal to more than half that of the wind-driven depth-dependent transport
- The observed spatially variable transport over the summer stratified period often opposed the direction of the wind-driven exchange

Supporting Information:
- Software S1

Correspondence to:
A. R. Kirincich,
akirincich@whoi.edu

Citation:
Kirincich, A. R. and S. J. Lentz (2017), The importance of lateral variability on exchange across the inner shelf south of Martha's Vineyard, MA, *J. Geophys. Res. Oceans*, *122*, 2360–2381, doi:10.1002/2016JC012491.

Received 20 OCT 2016
Accepted 24 JAN 2017
Accepted article online 9 FEB 2017
Published online 24 MAR 2017

1. Introduction

Visible beyond the surf zone, the inner part of the continental shelf serves as a connector between the nearshore, dominated by breaking waves, and the larger coastal ocean over the horizon, dominated by geostrophic and larger scale motions [*Lentz*, 2001]. The dynamics that control circulation in this region are decidedly different from that occurring both onshore and offshore [e.g., *Allen*, 1980; *Lentz and Winant*, 1986; *Lentz et al*., 1999] and yet critical to predicting the exchange across it. How this exchange occurs and what processes drive it affects the transport of water masses, nutrients, pollutants, and larval fish or invertebrates between the coastal ocean to the nearshore [e.g., *Menge et al*., 2003; *McGillicuddy et al*., 2005; *Dudas et al*., 2009]. While depth-dependent wind-driven upwelling or downwelling exchange has been quantified in detail [*Lentz*, 2001; *Kirincich et al*., 2005; *Tilburg*, 2003; *Fewings et al*., 2008; *Lentz et al*., 2008; *Fewings and Lentz*, 2011, among others], the role of lateral variably in modifying this exchange is poorly understood because of the difficulty of observing lateral variability at short scales using conventional mooring-based techniques. This study examines the spatial variability of transport within the inner-shelf south of Martha's Vineyard Massachusetts, its time and space dependence, and its importance to the total volume exchanged between the nearshore and the coastal ocean.

Dynamically defined as the part of the shelf where the surface and bottom Ekman layers overlap and interact [*Mitchum and Clarke*, 1986], the inner shelf has been studied primarily within a 2-D, along-shelf uniform framework (see review by *Lentz and Fewings* [2012]). Offshore, depth-dependent across-shelf transport due to wind-driven upwelling and downwelling dominates the exchange of water masses on many continental shelves [*Huyer*, 1990]. However, within the inner shelf, forcing due to across-shelf winds [*Tilburg*, 2003; *Fewings et al*., 2008] and waves, via the Stokes-Coriolis force [*Lentz et al*., 2008], can lead to higher magnitudes of volume transport than that possible via along-shelf wind-driven exchange alone, as overlapping boundary layers reduce the across-shelf transport within the inner shelf *Lentz* [1994]. Numerical model

results have illustrated the potential for local minima in exchange [*Austin and Lentz*, 2002; *Kuebel Cervantes et al*., 2003] within the inner shelf under both along-shelf wind forcing and wind forcing at an angle to the coastline [*Fewings et al*., 2008], suggesting that this area of the shelf can serve as an effective barrier, isolating the nearshore from the larger coastal ocean.

Along the coast, even small variations in bathymetry can lead to important deviations from the 2-D picture described above. Several examples of flow-topography effects [*Song et al*., 2001; *Tilburg and Garvine*, 2003; *Yankovsky and Chapman*, 1995] exist for the inner shelf and parallels to larger, shelf-scale variations [*Kirincich and Barth*, 2009a; *Castelao and Barth*, 2006; *Huyer et al*., 2005] can be made. More generally, lateral variability may be caused by bathymetric features, spatially variable wind forcing, coherent vorticities, or eddies, as well as incoherent horizontal stirring within the inner shelf. Yet relative to the depth-dependent exchange, which could be a local minimum in the inner shelf, the importance of these types of lateral variations on the total exchange has not been quantified. The lack of high-resolution observations of coastal flows at horizontal scales less than a few kilometers has been a barrier toward both quantifying the effects of lateral variability and improving estimates of both lateral stirring and energy transfer in the coastal ocean [*Capet et al*., 2008].

The inner-shelf south of Martha's Vineyard, Massachusetts (Figure 1) has been the site of recent efforts to examine both the 2-D exchange present and the role of lateral variability. Previous studies of 2-D exchange

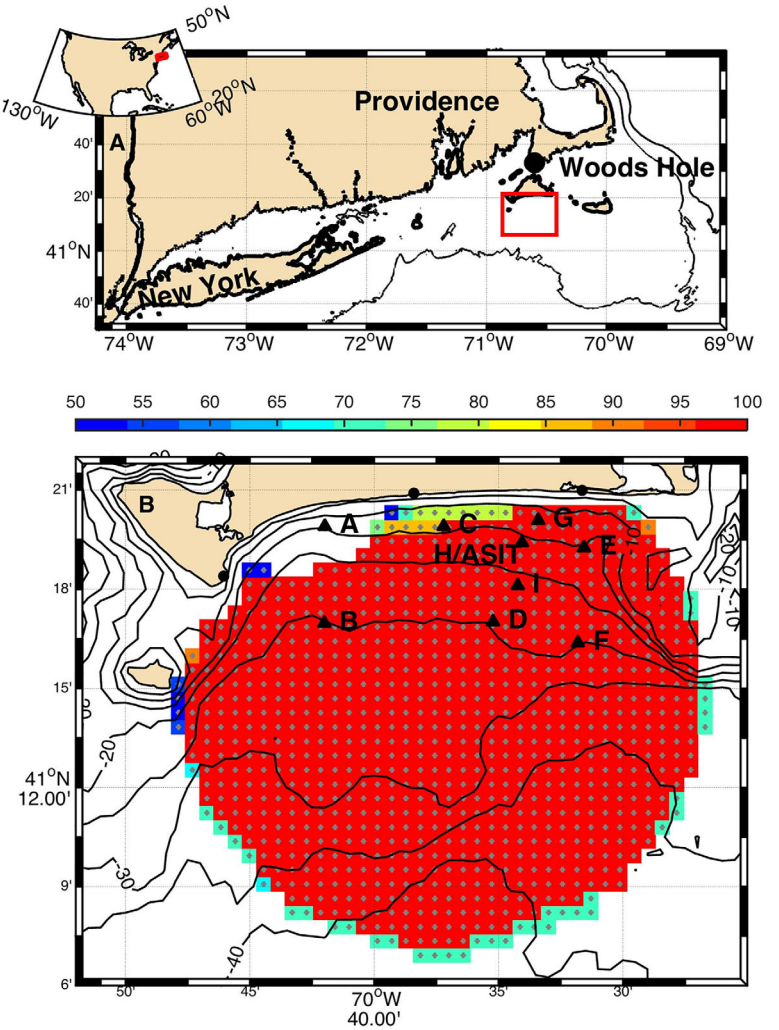

Figure 1. (a) The Southern New England Shelf denoted in red relative to North America (inset), and the study area south of Martha's Vineyard, Massachusetts (red box). (b) HF radar % coverage map with the locations of the radar stations (dots) and the ISLE moorings (triangles).

dynamics made using a single across-shelf array of moorings in the region observed strong coherence to theoretical transport estimates based solely on the wind [*Fewings et al*., 2008; *Horwitz and Lentz*, 2014]. *Fewings and Lentz* [2011] concluded that time-mean, nonwind-driven upwelling circulation cooled the inner-shelf south of Martha's Vineyard in summer. However, numerical model analysis [*Wilkin*, 2006; *Ganju et al*., 2011] and high-resolution high-frequency (HF) radar-based surface current observations [*Kirincich et al*., 2012] have found that the area is also subject to strong lateral gradients in tidal velocities due to the proximity of Wasque Shoals, a bathymetric shoal located between the islands of Martha's Vineyard and Nantucket. These lateral gradients in the tide lead to tidal rectification and a nonuniform low-frequency, or "background" circulation pattern. This pattern drives both sustained lateral gradients in across-shelf velocity and advective heat flux at the surface [*Kirincich et al*., 2012]. Additional analysis of the HF radar-based observations used by *Kirincich et al*. [2012] identified significant numbers of coherent vorticities or eddies with spatial scales of 2–5 km within a small (10 × 15 km) area due in part to wind forcing and tidal dynamics [*Kirincich*, 2016]. While focused on the structure and dynamics of the eddies occurring near Wasque Shoals, *Kirincich* [2016] also suggested that eddies had the potential to be an important means of lateral exchange for surface waters over the inner shelf. However, without knowledge of the vertical extent of the eddies, their full effect could not be quantified.

This study uses a combination of high-resolution HF radar surface current observations and a dense array of hydrographic and velocity moorings to examine the lateral scales of variability present on the inner-shelf south of Martha's Vineyard, MA and quantify the importance of these variations in relation to depth-dependent mechanisms for volume transport across the inner shelf. Relative to the surface current observations described by *Kirincich et al*. [2012] and *Kirincich* [2016], the radar deployment used here covered a broader spatial extent at slightly coarser spatial resolution. These data were collected during the Inner-Shelf Lateral Exchange (ISLE) study, which is described in detail below, followed by descriptions of the analysis methods used to estimate surface layer transports, identify eddies, and track particles. These data are then used to describe: the background circulation during the 6 month study period, the wind-driven depth-dependent exchange flow observed, and the occurrence of individual coherent vortex features or eddies. The across-shelf transport driven by each of these processes are quantified, and the results discussed in terms of their implications for the transport of water particles across the inner shelf. Thus, work focuses on the potential of wind-driven, eddy-driven, or mean processes to translate water masses across the shelf in a seasonally integrated sense, and does not include the potential effects of horizontal or vertical mixing on exchange.

2. Data

Conducted from 9 June to 4 December 2014, the Inner-Shelf Lateral Exchange (ISLE) study observed the in situ velocity and density structure at multiple locations in the inner-shelf south of Martha's Vineyard, MA, and paired these observations with high-resolution remotely sensed observations of surface currents made using land-based HF radar systems.

2.1. Subsurface Velocity and Hydrography

Observations of the vertical structure of velocity and hydrography were made at nine locations within the study area, spanning water depths of 12–25 m, 1.5–11.5 km offshore (Figure 1). At each location, a surface mooring supported 4–7 SBE-37 MicroCats measuring temperature and conductivity (CT) throughout the water column (Table 1). A nearby bottom lander supported an acoustic Doppler current profiler (ADCP) sampling water column velocities using vertical bins of 0.25–1 m and sample rates of 0.33–1 Hz. Moorings A, B, C, and F were deployed continuously from 9 June to 4 December while moorings E and I were deployed for 2 shorter time periods (Table 1) due to the constraints of a collaborative field program. The ADCP at mooring D was snagged by a trawler in mid-June and redeployed on 5 August. Mooring G is the Martha's Vineyard Coastal Observatory's (MVCO's) long-term underwater node, where continuous ADCP observations have been available since 2001. Mooring H, located adjacent to the MVCO tower itself, was deployed in early August. The CT observations were processed to remove both temperature and conductivity spikes as well as biases due to conductivity drift before being used to estimate salinity and density. ADCP along-beam velocities were processed following [e.g., *Kirincich and Barth*, 2009b] to give time series of quality controlled, horizontal velocities from 1 m above the instrument to 2–4 m below the sea surface due to

Table 1. The ISLE Mooring Array

	Location			Water			ADCP Bin
Mooring	Lat.	Lon.	Deployment Dates	Depth (m)	CT Depths (m)	ADCP Type	Size (m)
A	41°19.9115′N	70°41.9909′W	9 Jun 2014 to 2 Dec 2014	15	1, 3, 6, 9, 11	WH[a] 1200 kHz	0.5
B	41°16.9728′N	70°42.0058′W	9 Jun 2014 to 2 Dec 2014	25	1, 3, 6, 9, 12, 17, 21	WH 600 kHz	1.0
C	41°19.9113′N	70°37.2089′W	9 Jun 2014 to 2 Dec 2014	15	1, 3, 6, 9, 11	WH 1200 kHz	0.5
D	41°17.0233′N	70°35.2148′W	5 Aug 2014 to 15 Jan 2015	25	1, 3, 6, 9, 12, 17, 21	WH 600 kHz	1.0
E	41°19.2610′N	70°31.5581′W	2 Jul 2014 to 09/22/2014	15	1, 3, 6, 9, 11	NO[b] 1000 kHz	0.25
			11 Nov 2014 to 13 Jan 2015	15	1, 3, 6, 9, 11	NO 1000 kHz	0.25
F	41°16.3790′N	70°31.8090′W	11 Jun 2014 to 5 Dec 2014	25	1, 3, 6, 9, 12, 17, 21	WH 600 kHz	1.0
G	41°20.0931′N	70°33.4099′W	9 Jun 2014 to 31 Dec 2014	12	1, 4, 6, 9	WH 1200 kHz	0.5
H	41°19.4067′N	70°34.0606′W	6 Aug 2014 to 15 Jan 2015	16	1, 3, 6, 9, 11	NO 1000 kHz	0.25
I	41°18.1100′N	70°34.2297′W	2 Jul 2014 to 22 Sep 2014	21	1, 3, 6, 9, 12, 17	WH 600 kHz	1.0
			11 Nov 2014 to 13 Jan 2015	21	1, 3, 6, 9, 12, 17	WH 600 kHz	1.0

[a]T-RDI Workhorse Mariner or Monitor.
[b]Nortek 5-beam AD2CP.

sidelobe interference [*Gordon*, 1996]. The exact bin of the sidelobe masking was determined using a precise, signal intensity-based, estimate of the sea surface height that accounted for tidal variability of the water column. All moored time series were averaged over independent 1/2 h time intervals, centered on the hour, to match the temporal resolution of the surface current observations.

2.2. Surface Currents

For the ISLE study, the Woods Hole Oceanographic Institution (WHOI) high-resolution HF radar system [*Kirincich et al*., 2013] was reconfigured to observe surface currents within an expanded 30 × 40 km coverage area from May to December 2014. The three HF radar systems were spaced at ∼10 km intervals along the south coast of Martha's Vineyard (Figure 1). Each system was a 25 MHz Codar Ocean Systems SeaSonde direction-finding radar operated using a combination of 350 kHz bandwidth and low transmit power (10 W) to achieve resolutions of 429 m over ranges of 40 km. For each system, 1024 point (∼8 min) spectral estimates of the radar backscatter were used to resolve doppler velocities less than 0.01 m s^{-1}. Successive spectra were averaged using a moving 24 min averaging window to form an average spectral estimate every 15 min, which were processed using advanced methods [*Kirincich et al*., 2012; *Kirincich*, 2016] into quality controlled estimates of the radial velocity at radial and azimuthal resolution of 429 m and 5°, respectively. These data were combined into vector velocities on a uniform 800 m resolution grid via a weighted least squares technique using data within 1 km and successive 1/2 h time intervals centered on the hour. Only grid locations with an estimated Geometric Dilution of Precision (GDOP) [*Barrick*, 2002] of less than 1.75, or approximately 30° angular station separations, were used. Use of the logarithm of the estimated signal power as a weighting function increased the accuracy of the final product (Appendix A) and, when carried through the vector calculation, served as a superior indicator of velocity quality compared to standard error estimates based on the standard deviation of the radial velocity average.

2.3. Ancillary Data

Wind velocities and meteorological conditions were recorded by MVCO both at a shore-line based meteorological mast and an offshore tower (Figure 1). Winds from the tower, measured by a 3-axis sonic anemometer located at 17 m above the sea surface, were used primarily here, and are thought to be representative of winds over the entire study area. Small gaps in the tower wind record were filled using land-based sensors using transfer functions developed by *Fewings et al*. [2008]. Wind stress was estimated from the tower winds using bulk formulae [*Fairall et al*., 2003]. Estimates of the significant wave height and dominant wave period were estimated from the 2 Hz ADCP observations made at mooring G, following *Terray et al*. [1997].

3. Methods

3.1. Surface Layer Transport

The velocity profiles collected by the moored ADCPs were used to estimate the across-shelf transport within the surface layer following the methods described by *Lentz* [2001] and *Kirincich et al*. [2005], with a few key additions. At each mooring location, except mooring A, the observed HF radar surface currents nearest the

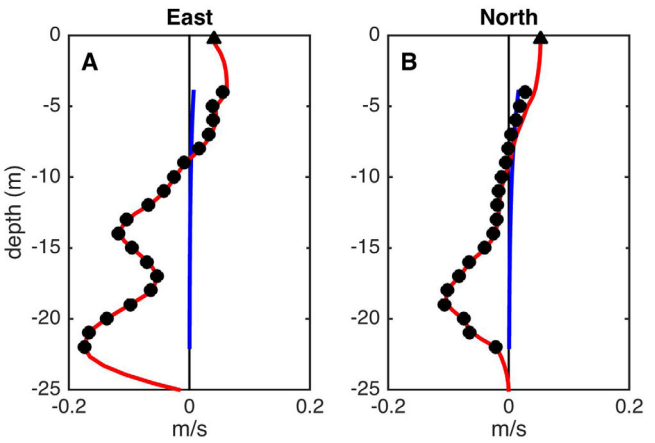

Figure 2. Sample vertical structure of the residual (tide and background mean removed) velocities incorporating both the ADCP and HF radar observations from lander B. Shown for the (a) east and (b) north velocities are the observed velocities from the ADCP (dots) and HF radar (triangle), the estimated Stokes drift vertical structure (blue), and the final interpolated velocity profile (red).

location of the mooring were combined with the subsurface velocities to create a full water column velocity profile for each 1/2 h of the full time series. At mooring A, which was not located within the radar coverage area, the velocity in the top 3 bins of the ADCP was extrapolated to the surface [following *Lentz*, 2001] to form the full water-column velocities. An estimate of the Stokes drift, which was measured by the radars but not by the ADCPs [*Kirincich et al.*, 2012], was added to the ADCP observations using the observed wave statistics [following *Lentz et al.*, 2008]. The added Stokes drift accounts for an important difference between the HF radar and ADCP data sets. Velocities were interpolated from the highest measured bin of the ADCP to the HF radar velocity at 0.5 m depth [*Stewart and Joy*, 1974], and from the bottom-most ADCP depth bin to 0 at the bottom (Figure 2).

To estimate the across-shelf transport, the full water column velocity profiles were rotated into a coordinate system aligned with the principal axis of flow, determined using the depth-averaged velocity after an estimate of the depth-averaged tidal flow, found using 8 tidal components and T_tide [*Pawlowicz et al.*, 2002], was removed. Estimates of (1) the depth-varying tidal flow, (2) the mean vertical structure of the across-shelf velocity, and (3) the depth-averaged across-shelf velocity were made and subtracted from the across-shelf velocities to obtain the across-shelf velocity anomaly at each mooring. The time-varying across-shelf surface transport was estimated by integrating the velocity anomaly from the surface to the first zero-crossing of the profile (Figure 2) deeper than 2 m depth and assuming a unit along-shelf width to yield time series of surface layer transport (U_{obs}, in m^3/s per along-shelf m) at each mooring. Tests comparing the surface transport results with and without the HF radar-based extrapolation to the surface found that accounting for the near-surface shear increases correlations with the theoretical wind-driven transports (shown below) by an average of 0.1 and 0.15 in summer and winter, respectively.

3.2. Coherent Eddies

3.2.1. Eddy Identification

Following a methodology described in detail by *Kirincich* [2016] and *Kim* [2010], this work defines an eddy as a set of closed contours of the stream function formed by the nondivergent horizontal stream function. The stream function and nondivergent velocities were isolated using a least squares fit to each independent 1/2 h residual velocity estimate—with the tide and temporal mean over the study period removed [*Kirincich*, 2016]—accounting for 70 ± 10% of the east velocity and 60 ± 10% of the north velocity components. The stream function interval used to find the eddy field was fixed at $\delta_\psi = 50\ m^2\ s^{-1}$ units for the data set (Figure 3). This defines the minimum circulation of an eddy, and is based on the potential error of the HF radar velocity estimates, generally 6 cm s^{-1} over the 800 m grid spacing (Appendix A). The method identifies only features that exceed a minimum change in stream function (i.e., intensity) that are larger than a minimum size (6 grid points for an effective minimum radius of ~2 km) and can be observed for longer than a minimum time period (1.5 h or three 1/2 h observations). The effective radius of the eddy was defined as the radius of a circle with an area equal to the area of the eddy. The center of the eddy was defined as the local minima or maxima of the stream function within the eddy. Eddies were tracked over time following [*Chelton et al.*, 2011], by assuming that the eddy area translated slowly enough to always overlap in space during subsequent observations.

3.2.2. Eddy Depths

The full velocity profiles available at the moorings were used to estimate the vertical structure of eddies when eddies were observed to pass over a mooring. For each realization of an eddy at a mooring, the vertical extent

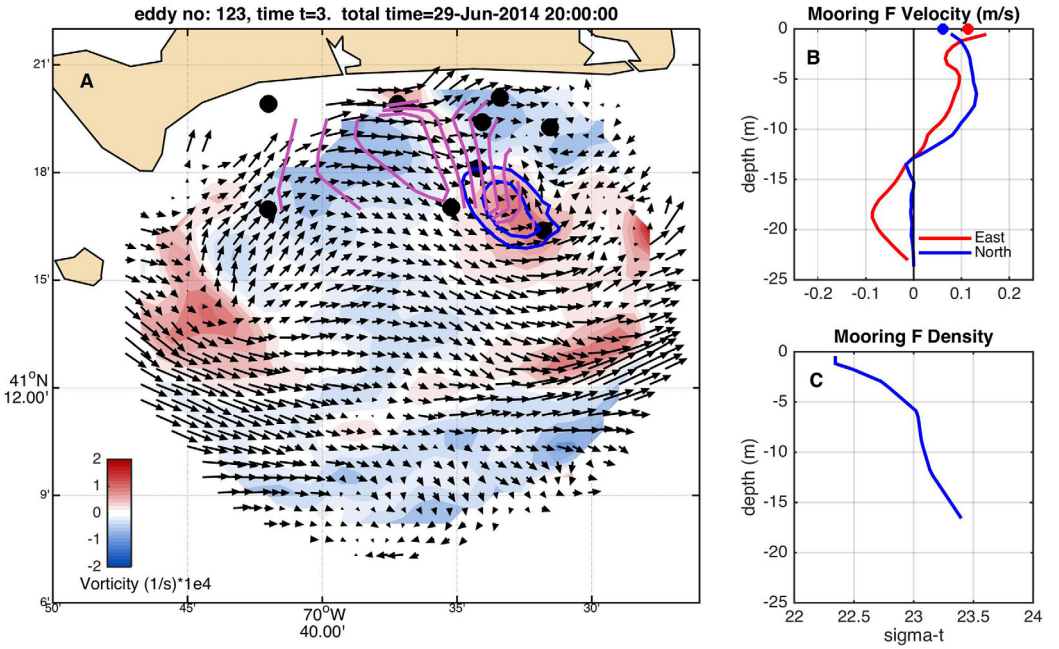

Figure 3. (a) Example of surface current velocity product (vectors) obtained on 29 June 2014 at 20:00 UTC. Overlaid on the vectors are the defined eddy streamlines (blue contours), vorticity (color), and density (magenta contours with contour interval of $\sigma = 0.02$). Additionally, the (b) vertical structure of the east and north velocity and (c) density measured at Lander F during the time of the eddy are also shown. For the example eddy, an eddy depth of 12 m was determined using the veering of the velocity vector from the surface as the defining criteria (see text).

of the eddy was determined from the veering angle of the horizontal velocity profile with depth below the surface. The depth at which the velocity veered more than 90° from the direction of the observed surface current was assumed to be representative of the thickness of the eddy itself. All available estimates of the eddy depth over the eddy lifespan were averaged to estimate the mean eddy depth. Additionally, the time-averaged eddy depth with radial distance away from the center of the eddy was estimated by tracking the eddy in an eddy-following coordinate system, and normalizing the distance to the center by the instantaneous effective radius of the eddy. Despite the dense spacing of the moorings, the number of eddies passing moorings was not sufficient to realize useful statistics on the change in depth of the eddy over its lifespan or the full horizontal variability of the eddy depth for individual eddies. The method used here was compared to methods using: different veering cutoffs (i.e., 45°), the depth to the first zero crossing of the dominant velocity component (Figure 3), and a change in density cutoff to define the eddy thickness. In general, velocity-based criteria were found to have reduced standard deviations for most eddy types (see below) than density-based estimates, and while differences existed in the absolute eddy depth results for individual threshold levels, the relative differences between eddy types were consistent across all methods.

3.2.3. Eddy Transport

Finally, pseudoparticles were seeded within the HF radar surface current results to track the movement of water starting within coherent eddies as well as establish the potential for transport across the shelf [*Rypina et al.*, 2016; *Kirincich*, 2016]. Particle tracking, utilizing the *HFR_Progs* Matlab toolbox which follows *Kaplan and Largier* [2006], was done for each eddy using two separate pseudodeployments: (1) particles starting at each HF radar grid point within all coherent eddies that overlap the 25 m isobath, and (2) particles starting at each grid point along a zonal line that spans the domain from east to west and passes through the center of the eddy. In each case, particles were advected over the lifespan of the eddy and each trajectory was assumed representative of a volume of water equivalent to an HF radar grid point in area (800 × 800 m) with a vertical extent equal to the mean eddy depth.

4. Results

4.1. 2014 Conditions

The ISLE study period spanned from early summer (9 June) to midwinter (4 December), 2014. Water column stratification, as estimated at lander D from the top to bottom density difference (Figure 4), increased from

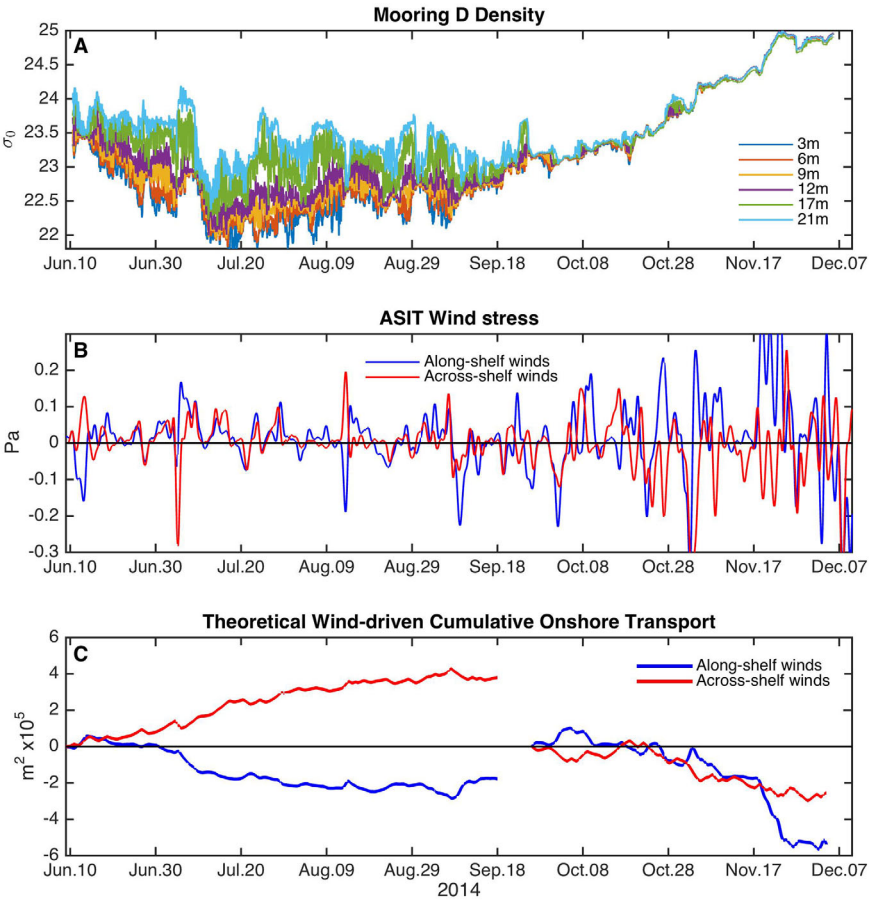

Figure 4. (a) Density at all depths (Table 1) observed at mooring D during the 2014 ISLE study period, (b) east and north wind stress calculated from the MVCO offshore tower wind observations, and (c) the theoretical, integrated wind-driven across-shelf transport in summer and winter (computed following *Lentz and Fewings* [2012]).

June until the beginning of August due mostly to changes in temperature (not shown here). On time scales of days, density and stratification varied in response to fluctuations in wind forcing. Westward (downwelling) winds generally resulted in reduced stratification (though not warming) while eastward (upwelling) winds led to increased stratification and in some cases cooling. However, large variations in density at time scales of multiple days occurred throughout the summer that were unrelated to wind events (i.e., 10 July or 1 September), suggesting that nonwind-driven subtidal processes were also present during summer [*Rypina et al*., 2014]. After mid-September, stronger wind events are correlated with decreases in stratification and increases in water column density (Figure 4) until the maximum density of $\sigma_\theta = 25$ is reached in December.

Wind stress over the inner-shelf south of Martha's Vineyard was predominantly to the northeast during summer [*Fewings et al*., 2008; *Kirincich*, 2016], defined here as the period between June and 18 September when the water column is normally stratified (Figure 4), with relatively mild wind stresses consistently between 0.05 and 0.1 PA. After the final breakdown of stratification on 26 September, defined here as winter, wind forcing is to the east or south east and stronger, with wind stresses generally greater than 0.1 PA [*Fewings et al*., 2008]. However, the standard deviation of the wind stress is greater than the mean throughout the year, with variability generally occurring on short, 1–5 day time scales (Figure 4).

4.2. Background Circulation

Previous model [*Wilkin*, 2006; *Ganju et al*., 2011] and observational studies [*Kirincich et al*., 2013] have documented the spatial structure of the seasonally varying background circulation in the region. Onshore and to the west of Wasque Shoals, a cyclonic recirculation pattern exists that is primarily driven by tidal rectification (Figure 5). However, this signal is modified by both seasonal stratification and low-frequency winds

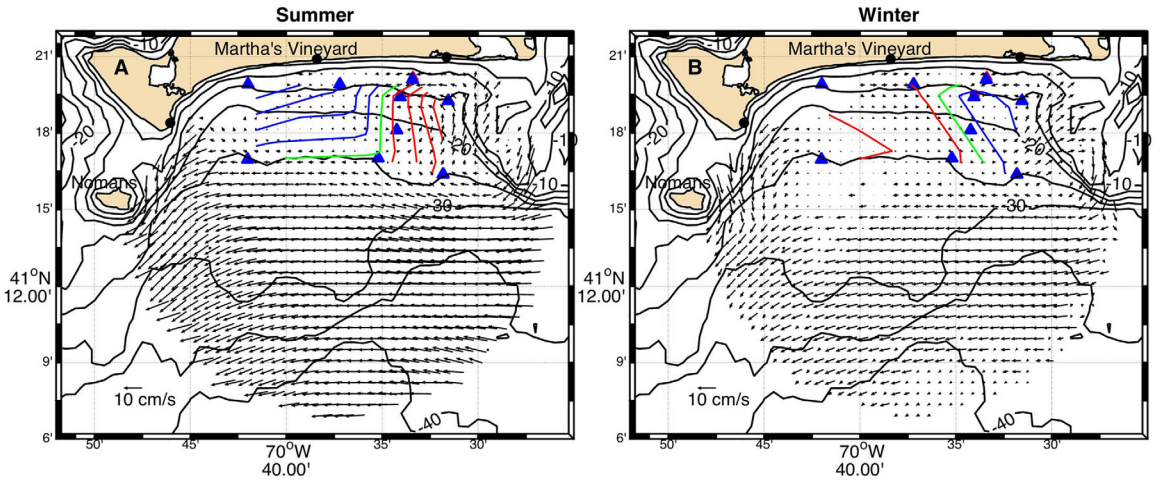

Figure 5. (a) Summer, 9 June to 18 September, and (b) winter, 26 September to 4 December, time averaged surface currents within the HF radar domain. Contours of the time-averaged density anomaly at 3 m depth, based on CT observations from the moorings, are overlaid with differences from the zero anomaly contour (green) shown in successive 0.025 σ_t positive (red) or negative (blue) contours. Thus, as shown, there is a 0.25 and 0.1 σ_t range in the mean density anomaly for summer and winter, respectively.

[*Kirincich et al*., 2013]. The size and intensity of the recirculation is larger and more intense during summer months, when winds are weak and horizontal density gradients are stronger, and weaker during winter when the density gradients are weaker. Inshore and west of this recirculation, mean surface velocities are weak except near the western end of Martha's Vineyard where stronger velocities exist near the gap between Martha's Vineyard and Nomans Island (Figure 5). Offshore and south of Nomans and the southern extent of Wasque Shoal, mean velocities are along-shelf to the west. However, evidence for a westward seasonal baroclinic jet, likely associated with horizontal density gradients emanating from Nantucket Shoals to the southeast [*Wilkin*, 2006], exists as the summer velocities are stronger and broader in spatial extent than in winter. This background circulation and its seasonal variations lead to differential transport of water masses as well as heat and salt along and across the inner shelf [*Kirincich et al*., 2013].

4.3. Wind-Driven Surface Layer Transport

The orientation of the principal axis of flow across the mooring array ranged from 30° to −33° relative to East (Table 2). Relative differences between the principal axis and the along-isobath direction was generally ±5° with the exception of moorings B and F (Figure 6), where the orientation of the principal axis crossed local isobaths by up to 60°. At B, the depth-averaged flow was potentially adjusting to the southwestward orientation of the 25 m isobath that exists west of the mooring due to the presence of Nomans to the southwest. At F, the flow could be constrained by the sharp bathymetry of Wasque Shoals rising to the east of the mooring. Importantly, at all moorings, the standard deviation of the along-shelf (major axis) depth-

Table 2. Wind-Driven Across-Shelf Surface Layer Transport Multiple Linear Regression Results

			Summer				Winter			
				Slope Due to Winds Directed				Slope Due to Winds Directed		
Mooring	Water Depth (m)	Principal Axis Direction (°)	Regression Intercept[a]	Along-Shelf	Across-Shelf	r[b]	Regression Intercept[a]	Along-Shelf	Across-Shelf	r
A	15	−9.3	−0.02	0.02	0.61	0.50	0.03	−0.09	0.32	0.67
B	25	29.5	0.03	0.30	1.11	0.63	0.01	−0.16	0.59	0.71
C	15	−0.9	−0.03	−0.04	0.95	0.70	0.02	−0.16	0.54	0.88
D	25	−15.6	−0.06	0.77	1.53	0.71	0.04	−0.20	0.65	0.75
E	15	−14.9	−0.02	−0.23	1.45	0.82	−0.02	−0.10	0.47	0.90
F	25	−33.5	−0.08	−0.01	1.37	0.68	0.02	−0.14	0.84	0.86
G	12	−7.0	−0.02	−0.18	0.87	0.81	0.02	−0.16	0.48	0.86
H	16	−2.7					0.02	−0.20	0.55	0.79
I	21	−21.5	−0.02	0.56	1.60	0.80	−0.01	−0.26	0.77	0.88

[a]In m^2/s per along-shelf m.
[b]Correlation coefficients significant at the 95% confidence level.

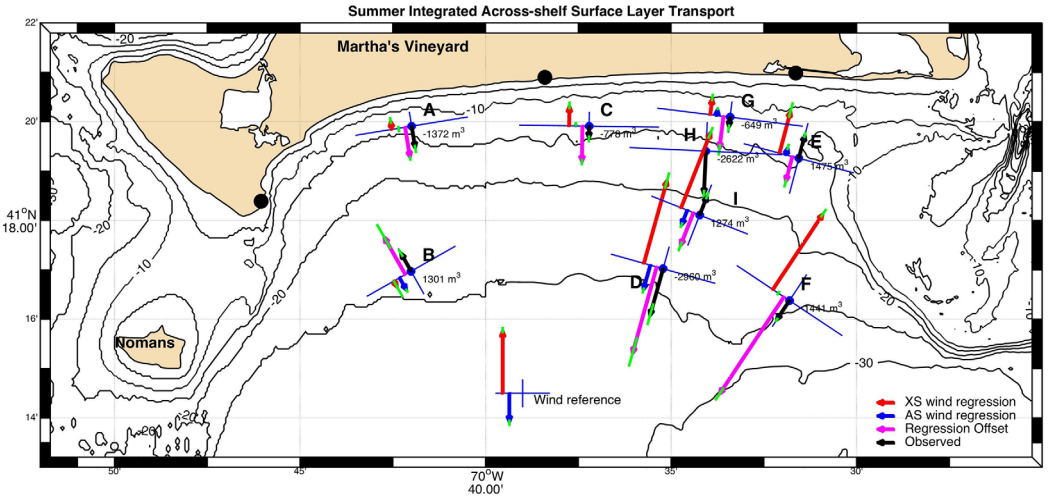

Figure 6. The along-shelf and across-shelf coordinate system (blue cross) at each ISLE mooring location is shown with the major and minor axis lengths scaled by the standard deviation of the depth-averaged velocities. On this axis, the time-integrated surface layer transport across the principal axis during summer (black arrows and listed in m^3 per day) is given along with the results of the multiple linear regression between the observed transport and the along-shelf and across-shelf winds (see text for details). The relative magnitude and direction of the integrated across-shelf surface transport due to the across-shelf (red arrows) and along-shelf (blue arrows) winds are shown as the integrated effect of the regression intercept (magenta arrows). Error bounds (green line) shown based on varying the principal axis $\pm 5°$ and recomputing all estimates. The theoretical transport for each wind component, derived from the observed winds (Figure 4), is shown for reference.

averaged velocity was generally twice or more the standard deviation of the across-shelf (minor axis) depth-averaged velocity (Figure 6: denoted by the relative size of the axis lengths at each mooring), suggesting that the principal axis results described here are robust.

A multiple linear regression was performed to estimate the components of the observed across-shelf surface layer transport (U_{obs}) driven by the along-shelf and across-shelf winds, respectively. Theoretical transports of the along-shelf and across-shelf exchange were estimated following *Lentz* [2001] and *Fewings et al.* [2008] as $U_{AS} = 0.25\tau_{AS}/\rho f$, for the along-shelf component, and $U_{XS} = u^* h$ for the across-shelf component, where ρ is a reference density, f is the Coriolis parameter, τ is the wind stress, $u^* = (\tau_{XS}/|\tau_{XS}|)|\tau_{XS}/\rho|^{1/2}$ is the friction velocity, and h is the water depth (Figure 4). The coefficient of 0.25 for the along-shelf Ekman transport has been previously found to represent the response of the inner shelf at these water depths to along-shelf wind forcing [*Lentz*, 2001; *Kirincich et al.*, 2005].

Across the domain, the predicted transport based on the regression was generally significantly correlated with the observed transport, accounting for 40–67% of the observed transport variance in summer (ignoring mooring A as an outlier) and 45–80% of the transport variance in winter. The regression coefficients themselves serve as indicators of how responsive U_{obs} was to each component of the wind. Regression coefficients for the along-shelf wind-driven transport increased with water depth as is expected from the results of *Lentz* [2001], but also varied with along-shelf distance, potentially due to the increase in stratification, although only the mean effect of stratification is considered below.

The breakdown of stratification that occurred after mid-September marked the transition to water column conditions representative of winter months, where boundary layers are expected to be deeper [*Lentz*, 1995]. During this period, across-shelf winds made the dominant contribution to the regression at all moorings (Table 2) likely due to the presence of thicker Ekman layers, but with regression coefficients that were generally half those found during summer. Regression coefficients for the along-shelf wind during winter were small, generally negative—or the opposite sign as what would be expected via Ekman transport—and unlikely to contribute to the positive correlation to the theoretical exchange observed.

During summer, the regressions at the 15 m moorings C, E, and G onshore favored forcing from the across-shelf winds, as across-shelf wind regression coefficients were 0.87–1.45 while along-shelf wind regression coefficients were near zero (Table 2). At D and I offshore, the summer regressions also favored forcing from the across-shelf winds, with regression coefficients near 1.6 while along-shelf wind regression coefficients

were smaller in comparison at near 0.6 (Table 2). At mooring F, the large rotation of the principal axis may have influenced the regression coefficients of the observed transport with the estimated wind-forced exchange. With a rotation that would put the dominant winds to the northeast more parallel to the across-shelf coordinate, the observed transport had a regression coefficient of near zero with the along-shelf wind-driven transport, but 1.37 with the transport driven by the across-shelf wind (Table 2). The rotation of the principal axis did not appear to alter regression coefficients at mooring B during the summer period. Despite having a principal axis more aligned with the dominant wind direction, the regression coefficient for the across-shelf transport due to along-shelf wind forcing was small (0.30) compared to the O(1) coefficient seen for the across-shelf wind-driven transport.

While these results show that theoretical estimates are indeed a reasonable predictor of the observed transport, especially during summer, the spatial variations in the regression values are as great as 50% of the values themselves, suggesting that strong gradients in wind-driven circulation can exist on spatial scales of kilometers. The lower correlation and regressions seen at A (Table 2) were due in part to its location outside of the radar domain that required a different surface extrapolation technique. Estimating the transport calculation using the nonradar extrapolation at mooring G (not shown here) gives regression correlations that are 0.2 lower than that shown in Table 2.

The regression intercepts represent the mean or integrated effect of the nonwind-driven transport observed at the mooring location. In general, the intercept is small relative to the size of the variations in the surface transport driven by the wind. For example, the standard deviation of the theoretical along or across-shelf transport driven by either wind component is O(0.1) $m^3\ s^{-1}$ per along shelf m, while the mean of the nonwind-driven transports are less than 0.03 $m^3\ s^{-1}$, except for at moorings D and F during summer. Notably, the mean nonwind-driven transports are directed offshore in the summer and onshore in the winter. While the magnitudes of the regression intercepts are small, they can have a sizable impact in the integrated depth-dependent transport observed at the moorings due to the fluctuating nature of the winds, as shown below.

4.4. Coherent Eddies

4.4.1. Occurrence and Distribution

Between 10 June and 5 December 2014, 635 eddies were identified within the footprint of the HF radar system. In general, statistics of the eddies identified (Figure 7) were similar for both anticyclonic and cyclonic eddies. Eddies tended to move less than 5 km from their starting point over their relativity short, 2–10 h, lifespans (Figure 7). The mean effective radius of the eddies had a peak at 1.5 km with a slow rolloff to radii of 3–6 km (Figure 7). Thus, most eddies do not translate horizontally more than their effective diameter.

Eddies are more often found in summer than winter, and the area adjacent to Wasque Shoals (Figure 8) dominates eddy activity in both seasons. Examining the spatial distributions of eddies during summer, eddy occurrences can be organized into approximately six "hot spots" of eddy activity, classified by both the location of the eddy and its rotational direction. Anticyclonic eddies were most often found within the (1) northeast corner adjacent to the Wasque Shoal (Figure 8), but also within a (2) broad area in the middle of the

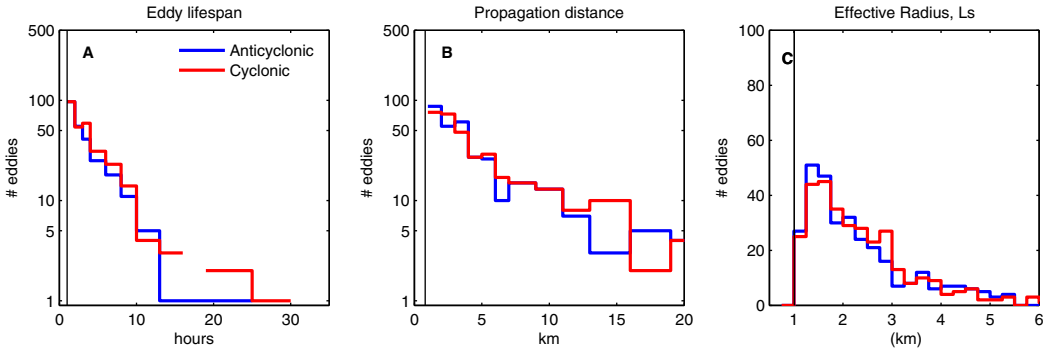

Figure 7. Eddy statistics including (a) eddy lifespan, (b) propagation distance, and (c) effective radius—as the radius of a circle having an area to that of the eddy. Note that a gap in the distribution of cyclonic eddy lifespans exists as no observed eddies were found within that time range.

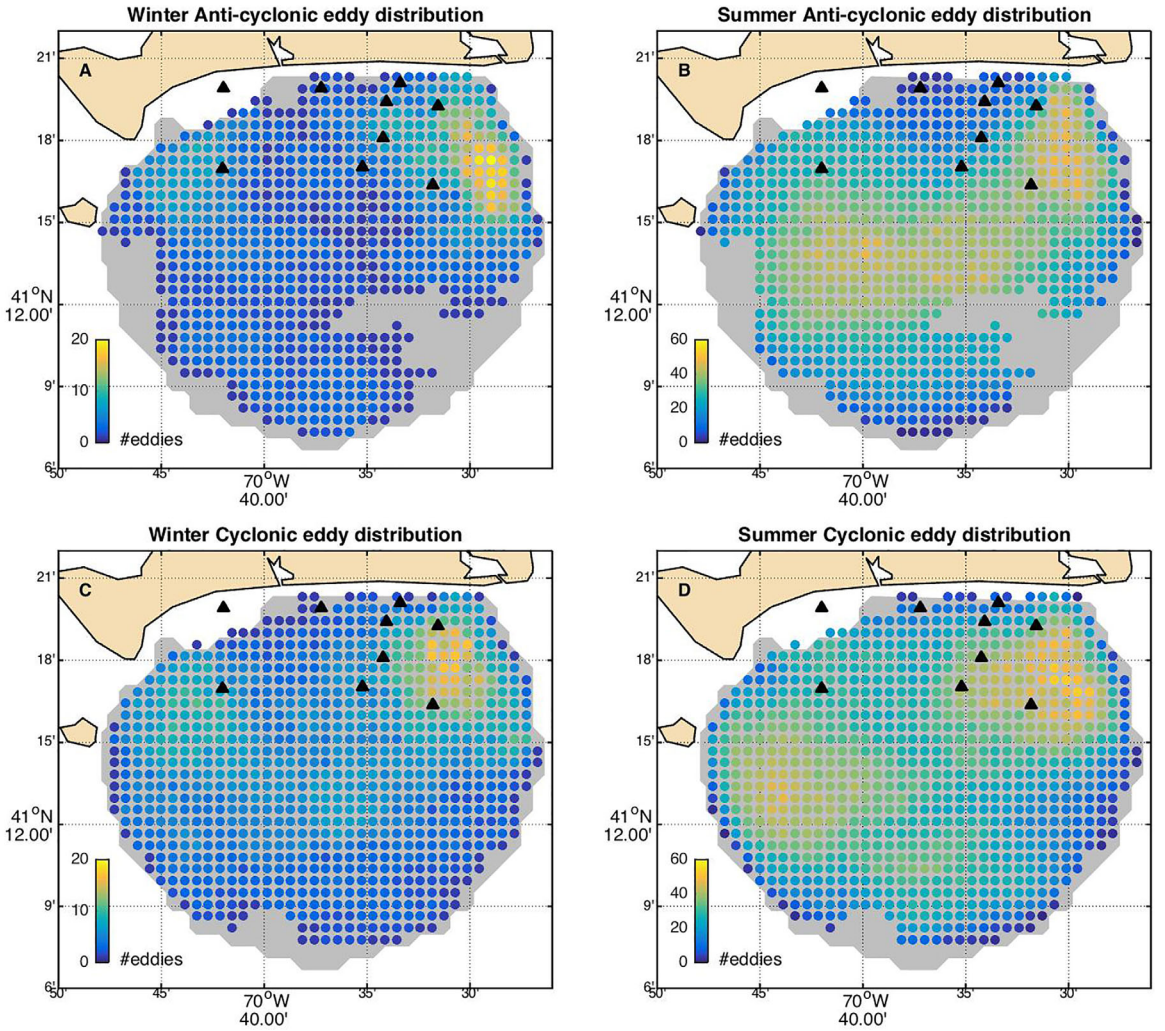

Figure 8. Eddy density, defined as the number of eddies seen at a grid point for (a, b) anticyclonic and (c, d) cyclonic eddies during (a, c) winter—26 September to 4 December, 2014—and (b, d) summer—10 June to 18 September, 2014. Note the range of the color bar is different for winter and summer.

domain, located approximately inshore of the main axis of the along-shelf coastal current present during summer (i.e., Figure 5). A notable portion of this broad area of anticyclonic eddies is adjacent to the (3) western edge, centered at 41°13′N, 70°44′W. Cyclonic eddies were found within an expanded portion of the (4) northeast corner as well along the (5) western edge and (6) offshore of 41°12′N, south of the main axis of the along-shelf coastal current during summer (Figure 1).

4.4.2. Characteristic Eddy Types

The six eddy types, defined above and in Table 3, account for 529 of the 634 eddies identified. Each represent a characteristic flow field of the study area as can be seen in a composite average of the velocity fields during each eddy type (Figure 9). It is important to note that the focus here is not solely on the eddies themselves but the characteristics of the larger flow field observed in the domain when eddies are present. Averaging in geographic coordinates, as done here, has the effect of smearing the spatial structure of the eddies out over a slightly larger area than the mean eddy diameter for each eddy type due to the variable diameters and centroid locations of the eddies (Figure 9). However, forming this composite view using an eddy-centric reference frame, normalize by the mean eddy radius, gave a qualitatively similar result as that shown here for the circulation of the eddies themselves, but had the larger negative effect of biasing the far-field flow structures.

Anticyclonic and cyclonic eddies in the northeast corner (Figures 9a and 9d), encompassing those previously described by *Kirincich* [2016], are the most numerous but generally have smaller effective radii and

Table 3. Characteristic Eddy Type Statistics

Rotation	Location Definition	# Eddies	Effective Radius (km) Mean	Effective Radius (km) Std. Dev.	# Eddies w/depths[a]	Eddy Depth (m) Mean	Eddy Depth (m) Std. Dev.
Northeast corner							
Cyclonic	North of 41°15′, East of 70°36′	139	2.1	0.8	84	8.4	0.5
Anticyclonic	North of 41°15′, East of 70°33′	120	1.9	0.6	55	6.8	0.7
Western border							
Cyclonic	South of 41°17′, West of 70°40′	86	2.7	1.2	18	13.2	1.4
Anticyclonic	North of 41°15′, West of 70°37′	55	2.3	1.1	26	6.8	1.3
Offshore							
Cyclonic	South of 41°12′, East of 70°42′	47	2.7	1.2	5	9.1	2.4
Anticyclonic	South of 41°15′, West of 70°33′	82	2.9	1.2	12	8.9	1.6

[a]The number of eddies of each type observed passing a mooring, yielding an estimate of the eddy depth.

shorter lifespans relative to those identified elsewhere within the domain (Table 3). The dominant nontidal flow present at scales larger than the eddy is strong and to the northwest (southeast) for anticyclonic (cyclonic) eddies, suggesting that the eddies themselves are wedged between this cross-isobath flow and Wasque Shoals to the east. Examining the mean composite near-surface (3 m) density anomaly, formed by removing the spatial structure of the monthly mean density spatial anomaly (Figure 5) from the spatial anomaly of density during all eddies of each characteristic type, the composite eddy anomaly was near zero for cyclonic eddies within the northeast corner but had a $\sigma = 0.04$ difference across the western side of the composite anticyclonic eddy, with denser waters located within the eddy core.

Eddies along the western edge (Figures 9c and 9f) appear to interact strongly with both the western edge of Martha's Vineyard and Nomans to the south. Cyclonic eddies of this type are tightly distributed just east of Nomans and tend to occur during winds to the north with strong onshore surface currents throughout the domain east of the eddy. Anticyclonic eddies in the northwest corner are more diffuse in location, have

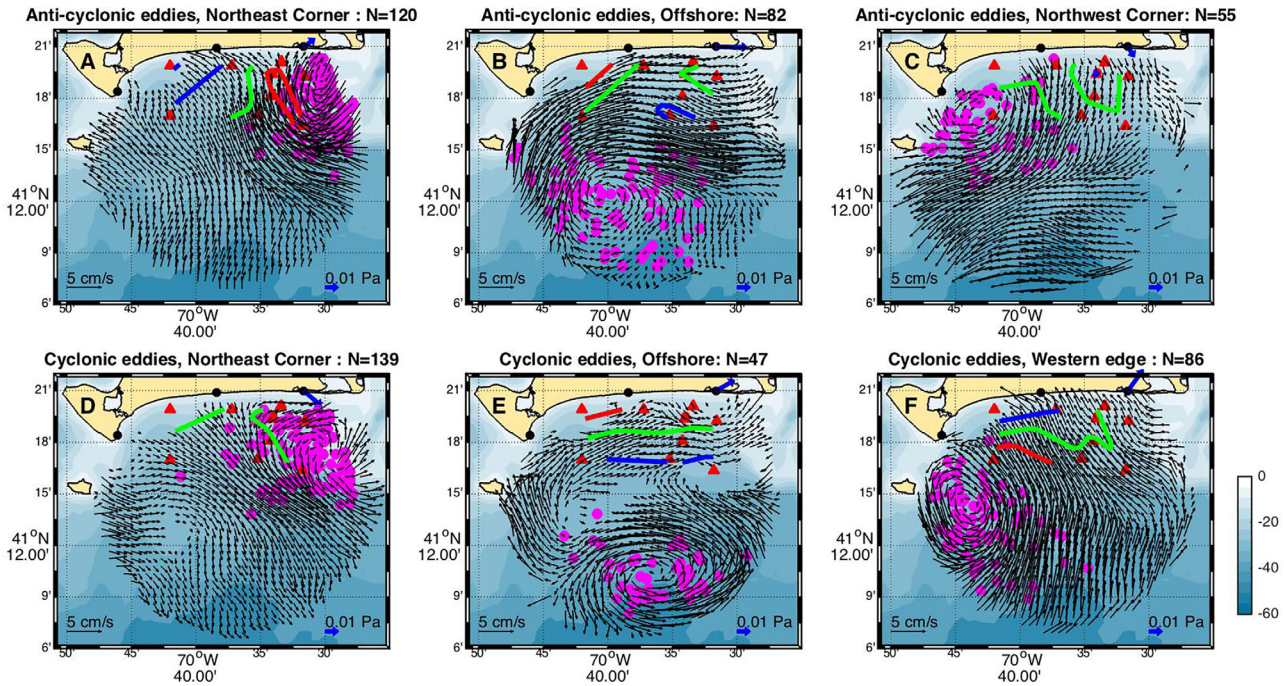

Figure 9. Composite surface currents present during each of the six characteristic eddy types (Table 3). For each plot, the time-averaged surface currents present over the life of each eddy are averaged for all eddies within each eddy type (Table 3). Only eddy averaged mean currents that are larger in magnitude than the standard error are shown. Additionally, the mean location of the center of each eddy (magenta dot) within the characteristic type are shown to illustrate the potential smearing of the composite surface current field due to the spatial variability of the eddy locations themselves. Superimposed on the velocity fields are the eddy averaged density anomaly contours at 3 m depth (with a contour interval of $\sigma_t = 0.02$) formed by removing the seasonally varying background density structure shown in Figure 5 from the instantaneous densities estimated at the moorings. The composite-averaged wind stress, observed at the offshore tower near mooring H (Figure 1), is shown at the location of the shoreline-base meteorological mast for clarity (thick blue arrow).

relatively small effective radii, weak density anomaly gradients, and are associated with strong surface flow offshore to the southwest, but relatively weak winds.

Eddies found offshore (Figures 9b and 9e) are the largest of all of the eddies observed (Table 3), for both rotational directions. Average winds were strong and to the northeast during occurrences of offshore eddies, and surface currents onshore at the moorings were to the east and consistent with the observed density anomaly gradients (see below). Offshore, the composite flow suggests an along-shelf jet exists onshore of both eddy types. However, the locations of the anticyclonic offshore eddies are fairly diffuse to the south, likely influencing the composite view more for this eddy type than for other composites.

4.4.3. Eddy Depths

Estimated depths for most eddy types were similar, to within the standard error of the mean eddy depth, particularly at 1–1.5 radii away from the eddy center. Inside of 1 radii from the center, cyclonic eddies found along the western edge had the deepest depths, at 10–18 m 0.5–1 radii away from the center, the approximate sill depth between the western edge of Martha's Vineyard and the Nomans Island offshore to the south (Figure 1). Cyclonic eddies in the northeast corner also had slightly greater eddy depths than the remainder of the eddy types, with values of 10–12 m at 0.25-0.5 radii from the eddy center, similar to the shoal depth directly to the east. Due to the velocity-based detection method used, eddy depths are likely to be biased shallow when detected at the center of the eddy where flow is the most quiescent and velocity errors might lead to increased veering with depth. In general, depth estimates were possible at less than half of the eddies for most eddy types (Table 3). While depths were available for 60% of the cyclonic eddies in the northeast corner due to their proximity to the moorings, only 10% of the cyclonic eddies offshore were seen at the moorings. Similarly, it should be noted that only the largest offshore eddies were observed at the moorings and most of these depth estimates were at the eddy edge.

4.4.4. Eddy Drivers

Winds: While no clear relationship to wind speed exists for eddy formation, as was found by *Kirincich* [2016] for the northeast corner of the present study area, wind direction does play a role in determining when and where eddies will normally form. Cyclonic eddies form along the western boundary predominately during winds to the northwest (Figure 10b, blue dots), where the larger flow field around the eddy is strong and onshore directed at the surface (Figure 9). In contrast, anticyclonic eddies forming during northwestward winds are most often found in the northeast corner (Figure 10a, blue dots). Comparing the composite eddy structures with the direction of the wind and surface flows for these eddy types suggests that eddies during northwestward winds might form predominantly due to blocking of the wind-driven flow by local topography. During winds to the northeast, both eddy types are more widely distributed, with the exception of a local minimum in eddy activity along a northwestward line across the domain (Figure 10). In many of the eddy types, the strongest composite velocities are found along this line, suggesting this is the general position of the along-shelf coastal current described by *Wilkin* [2006] during eddy generation (Figure 9). However, winds to the northeast are the dominant wind direction during summer [*Kirincich*, 2016] and thus some

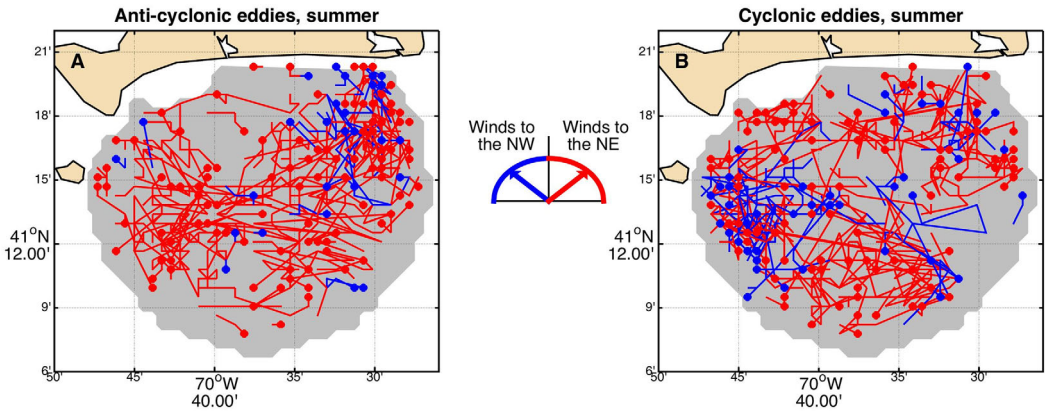

Figure 10. The starting location and total track line of the center of all (left) anticyclonic and (right) cyclonic eddies present during summer. Eddy tracks are colored by the direction of the wind forcing during the time of the eddy, where red tracks occur during times of winds to the northeast and blue tracks occur during times of winds to the northwest.

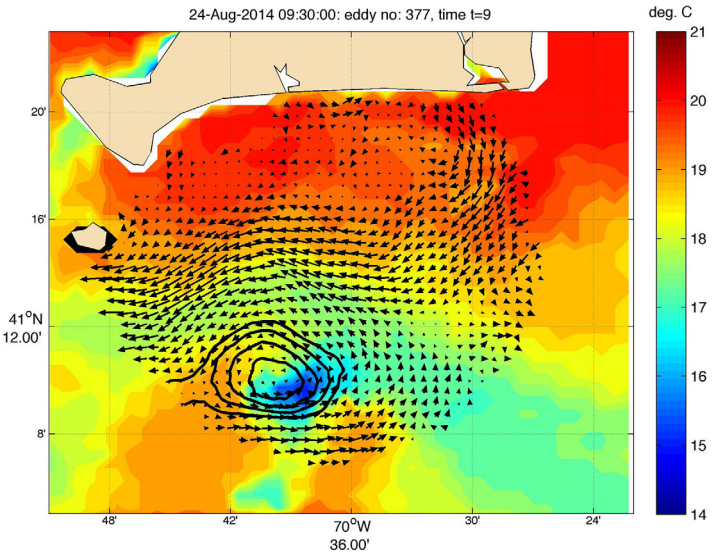

Figure 11. Example of a cyclonic offshore eddy with coincident and clear SST imagery found on 09:30 GMT, 24 August 2014. Eddy streamlines (black lines) are shown over the residual (with both the tide and the monthly mean removed) surface current field. The SST imagery was downloaded from www.maracoos.org and reprocessed to mask for land, clouds, and correct for georectification errors.

of the processes leading to the distributions seen for northeastward winds might not be due to the wind itself.

Tides: A fraction of the eddies in the northeast corner appear to be linked to the phase of the M_2 tide as eddies of both rotational types are more likely to occur at max flood or ebb than other phases of the local tide. As illustrated by *Kirincich* [2016], this is of interest as simple vortex stretching of tidal flows [*Robinson*, 1981] does not account for the generation of cyclonic and anticyclonic eddies on both ebb and flood tide conditions, but suggests a more complex spatial structure of tidal phase. However, eddies in the northeast corner do occur at all phases of the tide, suggesting that a large portion of the composite structure seen in (Figure 9) might be due to nontidal effects such as the wind effects described above. Along the western boundary, in proximity to stronger tidal flows between Martha's Vineyard and Nomans, cyclonic eddies occur twice as often during times of slack water as observed at mooring B, in contrast to the link between maximum tidal flows and eddies in the northeast corner.

Horizontal Density Gradients: Near-surface gradients in density within the composite eddy averages (Figure 9) are generally weak except for during anticyclonic eddies in the northeast corner and offshore eddies. For anticyclonic eddies in the northeast corner, composite surface velocities in the eastern part of the study area are onshore and, despite appearing to be along lines of constant density anomaly (Figure 9), against the direction of a thermal wind shear between the horizontal density gradient and the velocity field, assuming weak flow at the bottom. For the eddies found offshore, the flow located in and around the mooring locations appears to be along lines of constant density anomaly (Figure 9), and has a direction consistent with a thermal wind balance. With a composite 0.04 kg m^{-3} density change between the 15 and 25 m moorings (a 5 km separation), the thermal wind velocity would be ~2 cm/s at the surface, similar to the observed velocity magnitudes. Farther offshore at the locations of the offshore eddies, anecdotal evidence from the small number of eddies with concurrent cloud-free SST imagery suggests that density gradients or baroclinic processes are a potential driver for these eddy types. For example as shown in Figure 11, a cyclonic eddy exists along the offshore edge of a plume of cooler waters meandering through the study area.

4.5. Transport Comparisons

The relative importance of wind-driven transport, eddy-driven transport, and the spatial variability of the background mean flow on exchange across the inner shelf can be quantified by integrating the volume of water predicted to move across the shelf—represented here in units of m^2/d (i.e., m^3/d per along-shelf m) due to each process. Estimates are given separately for the periods before 18 September (summer) and after 26 September (winter), defined based on the final breakdown of stratification that occurred between the 18 and 26 September (Figure 4).

4.5.1. Wind-Driven Depth-Dependent Transport

The observed across-shelf and along-shelf winds have competing influence on the direction and magnitude of exchange across the shelf during summer (Figure 4). The average theoretical across-shelf transport due to the across-shelf winds would result in 3762 ± 120 m^2/d of volume transport directed onshore, while the

theoretical effect of the along-shelf winds would provide 1760 ± 120 m^2/d of volume transport directed offshore (Figure 6). Uncertainty estimates for both wind-driven transports were assessed by assuming a potential bias in the wind speed of up to ±0.1 m/s and computing the subsequent range of wind-driven transports. Both wind components would, in theory, result in offshore exchange in winter with most of the theoretical transport driven by along-shelf winds as a result of two large wind events in mid-October and mid-November, respectively (Figure 4).

For the observed across-shelf surface layer transport driven by the summer or winter winds, the regression coefficients shown in Table 2 were used to predict the average transport realized at each mooring due to the along-shelf and across-shelf wind forcing. Using this approach, the potential effect of the winds are integrated over the full season for all moorings, even though observations at the moorings might be shorter in length (i.e., D, H, E, and I in Table 1). The potential range of uncertainty present was estimated by varying the orientation of the principal axis of flow, a critical component of the across-shelf transport calculation, at all moorings by ±5° and recalculating the regression results and the average transports.

The average transport driven by along-shelf or across-shelf winds varies systematically across the mooring locations (Figure 6). During summer, both the across-shelf and along-shelf wind-driven transport change sign from B to F, or west to east. As the local winds are rotated into along-shelf and across-shelf coordinate system at each location, a portion of the differences seen—particularly the near-zero along-shelf wind-driven exchange at F—was likely due to the difference in principal axis orientation, defined by the depth-averaged, nontidal flow. Yet, the increased across-shelf wind response seen at moorings D and F relative to B exists even with no coordinate system rotation (not shown here). Onshore at the 15 m moorings (A, C, G, and E), the across-shelf wind-driven exchange generally increases fivefold from 547 ± 130 to 2642 ± 400 m^2/d directed onshore from west to east, while the along-shelf wind-driven exchange was weak in comparison, varying from ±100 m^2/d at A and C to 400 to 500 m^2/d directed onshore at G and E. During winter, strong offshore transport driven by the across-shelf winds exists at all moorings, with magnitudes of 1200–1800 m^2/d at the 15 m moorings, and up to 3800 m^2/d at moorings B and D in 25 m of water. As regressions of the observed transport against the potential along-shelf wind-driven exchange were uniformly weak (Table 2) with the opposite sign to that expected due to Ekman transport during winter, they are not considered further.

The observed mean transport (Figure 6: black arrows), the time integral of U_{obs} within the surface layer divided by the duration, also had sizable lateral variations over the summer. At the 25 m moorings, observed transport ranged from 1300 m^2/d directed onshore at B to 1300 m^2/d offshore at F. At the 15 m moorings, observed transports were up to ±1300 m^2/d and directed offshore at all moorings but E, where onshore flow was observed. This observed transport pattern reversed during the winter season with strong, 2600 m^2/d, offshore transport at B but 1800–2500 m^2/d onshore transport in the east at D and F. The observed transport at the inshore mooring was between 1000 and 2000 m^2/d onshore at all stations but E, where offshore transport was observed.

The average transport due to the regression intercept (Figure 6: magenta arrows) can be thought of as the integrated effect of all other nonwind-driven processes that also drive depth-dependent exchange. As can be seen in Figure 6, this transport generally represents the difference between the combination of the wind-driven transports, based on the regressions between the wind and the surface layer transport, and the observed transport. During summer, this transport was directed offshore with variable magnitudes near ~2000 m^2/d at 15 m and ~6000 m^2 at D and F, but onshore at mooring B in the west. During winter, this transport was directed onshore at all moorings except E (not shown here).

4.5.2. Eddy Transport

Tracking particles that start within the eddy over the lifespan of the eddy serves as an estimate of how eddies—defined solely by their stream function—trap and move water parcels. This calculation focuses on eddies that were seen along the 25 m isobath, as direct estimates of their vertical extent observed at moorings B, D, F, or I can be used to estimate the volume transport. Following *Kirincich* [2016], the eddy across-shelf volume transport was estimated by integrating the northward (effectively onshore) volume transport of all seeded particles for each eddy, assuming each particle was representative of a volume of water equivalent to an HF radar grid cell (800 m × 800 m) with the same vertical extent as the eddy. However, given that most eddies do not translate far relative to their diameter, the ability of an eddy to move a particle of water from one side to the other over its lifespan, defined here as its relative transport, represents a source

Table 4. Daily Averaged Across-Shelf Transport by Eddies[a,b]

	Summer			
	Eddy		Line	
Eddy type	Mean	Relative	Mean	Relative
Anticyclonic	−155 ± 36	546 ± 365	∼0	1413 ± 910
Cyclonic	−161 ± 43	556 ± 375	∼0	1443 ± 942
	Winter			
	Eddy		Line	
Eddy type	Mean	Relative	Mean	Relative
Anticyclonic	−421 ± 172	221 ± 126	∼0	333 ± 176
Cyclonic	118 ± 80	181 ± 100	∼0	254 ± 125

[a]In m^3 per along-shelf m, or m^2, per day.
[b]See discussion for calculation details.

of exchange across the shelf in addition to the simple translation of the eddy as a whole. This rotational effect can be estimated via the sum of the displacement, relative to the mean displacement, of all parcels that move farther onshore than the mean. For both calculations, results were normalized by the domain width, or the along-shelf extent of the study area at the location of the eddy center, to yield a volume transport (m^3 per m in the along-shelf direction) that is summed for all eddies of a characteristic type and divided by the duration of the season to yield an average transport, in m^2 per day, that is directly comparable to estimates of the wind-driven transport. The potential uncertainty of the eddy transports were assessed by varying the estimated eddy depths by the standard deviation of eddy depths for each eddy type and estimating the range of transports that would result (Table 4).

Within the domain, eddies generally moved offshore during summer, thus the eddy mean or translational effect transports volume offshore with cyclonic and anticyclonic eddies contributing roughly equal amounts (Table 4). During winter, anticyclonic eddies move predominate offshore, driving a larger offshore transport than the onshore transport due to cyclonic eddies. Integrated over the summer, the total translational effect of the eddies alone (316 ± 79 m^2/d directed offshore) accounted for exchange equal to 25% of the observed wind-driven depth-dependent exchange across the 25 m isobath (1280 ± 233 m^2/d directed onshore) but in the opposite direction (Table 5). During winter, eddy-driven transport is offshore, 1/3 the magnitude of, and in the same direction as the wind. The relative effect of eddies contributed an additional $\sim 550 \pm 370$ and $\sim 200 \pm 370$ m^2/d of volume transport for both rotational directions for summer and winter respectively (Table 4).

As shown by *Kirincich* [2016], coherent eddies in the study area generally exist as local minima of eddy kinetic energy within the flow field. Thus, how much of the total relative exchange observed occurs within the defined eddy itself, as opposed to outside the eddy, is an important aspect of this calculation. Advecting particles starting along an along-shelf line centered at the 25 m isobath over the lifespan of each eddy allows an estimate of how much of the rotational effect caused by the eddy was located inside the eddy. During summer, the relative volume transport of the line particles was almost three times the relative transport of the in-eddy particles for both eddy types (Table 4), and thus the eddy itself accounts for only a fraction of the relative volume exchange due to the conditions that lead to eddy formation. In contrast, the

Table 5. Average Observed Transports Across the 25 m Isobath[a,b]

	Wind		Eddy		Background	
	Mean	Relative	Mean	Relative	Mean	Relative
Summer	1280 ± 233	1960 ± 468	−316 ± 79	1101 ± 740	264 ± 121	3426 ± 853
Winter	−970 ± 285	849 ± 750	−303 ± 252	402 ± 226	2183 ± 143	4029 ± 853

[a]In m^2 per day (m^3 per along-shelf m per day).
[b]See discussion for calculation details.

relative volume transport of the line particles was only slight more that the eddy relative transport in winter, suggesting that most of the exchange effects were confined to the eddy itself.

4.5.3. Background Transport

The spatial mean cumulative transport of the background flow field (Figure 5) can be similarly estimated by integrating the monthly averaged velocity structure, which was removed from the residual velocities used to estimate depth-dependent transport and eddy transport, over the summer and winter periods. A mean surface layer thickness of 5 m is assumed for consistency with the above estimates of eddy depth, and uncertainty estimates for the background transport were made by propagating the standard error of the mean and anomaly fields. Applied to an east-west line, approximately along-shelf, centered at the 25 m isobath, the spatial mean background exchange was small relative to the wind-driven and eddy-driven exchange in summer, but large and opposite to the wind-driven and eddy-driven exchange in winter (Table 4). In both seasons, the relative exchange due to the background flow field was 1–2 times larger than all other sources of relative exchange.

5. Discussion

5.1. The Drivers of Depth-Dependent Exchange Variability

The across-shelf surface layer transport is used here as an indicator of how variable inner-shelf circulation can be within the study area. The combined use of HF radar surface currents and moored ADCP results represents the best estimate of the true surface layer transport because of its ability to capture near surface shear. Across the mooring array, the surface layer transport varied dramatically, up to 100% of the theoretical wind-driven response, likely because of variability in wind-driven and nonwind-driven transport processes. Both are discussed further here.

Establishing the local coordinate system was critical to most aspects of the analysis, hence its use in estimating the transport uncertainties. Rotating observed velocities into an along-shelf and across-shelf coordinate system based on the principal axis of the depth-averaged flow has been utilized for some time [e.g., *Kundu and Allen*, 1976] to understand the effects of the wind on across-shelf dynamics relative to the more dominant along-shelf dynamics. However, in the context of a larger number of mooring locations with variable bathymetric conditions, it is unclear if a more appropriate definition for along-shelf is necessary. In general, small rotations of the principal axis can have large results in the estimated transport, particularly at the offshore moorings. Offshore, the relative angle between the principal axis and the dominant wind direction varied by up to 50°, and thus was a factor in determining the regression magnitude and direction of the wind-driven surface layer transport. However, estimating the regression between the surface layer transport and wind-driven transports on a nonrotated, east and north coordinate system, there are still differences in the regression coefficients of up to 50% over relatively small spatial scales (not shown here). Thus, the definition of along-shelf is not the only reason for the differences seen.

Independent of the coordinate system itself, differences from the predicted transport are likely due to either variations in stratification, which would drive a different magnitude response in the surface layer, or differences in the winds themselves. While the spatial variability of the wind was not measured at multiple offshore sites, comparing wind observations from mooring H to land-based sensors up to 10–15 km away found only small differences during times of onshore winds, which include the dominant wind direction out of the southwest. However, there are notable spatial variations in the mean stratification that partially explain the spatial trends in the response to the wind found in summer. The time-mean top to bottom stratification decreases from 0.04 to 0.028 kg m^{-3}/m moving from west to east along the 15 m isobath along with the increase in the across-shelf wind regression coefficient (Table 2). Offshore moorings have mean stratifications of ~0.05 kg m^{-3}/m except F, which at 0.038 kg m^{-3}/m is more similar to the 15 m sites in stratification magnitude and regression coefficients. As discussed in *Lentz and Fewings* [2012], decreased stratification at a given water depth would favor a stronger response to the across-shelf wind forcing than that seen for the along-shelf winds. This shift toward a larger response to the across-shelf wind as well as the difference in principal axis orientation, might account for the differences between F and the other offshore moorings.

5.2. The Drivers of Eddies

With mean transport magnitudes up to 1/3 of the wind-driven exchange, coherent eddies appear to be an important component of the lateral exchange observed south of Martha's Vineyard. As shown by *Kirincich*

[2016], a fraction O(40%) of the eddies occurring within the northeast corner were linked to specific phases of the local M_2 tide that are conducive to the generation of vorticity due to vortex stretching [i.e., *Robinson*, 1981]. However, whether an eddy is found within the northeast corner appears to also depend on wind direction (Figure 10). The spatial extent of the eddy hot spot within the northeast corner is not significantly different between winter and summer, and is similar in along-shelf and across-shelf extent to that of the shoals itself. Thus, while differences in wind forcing and stratification appear to affect the total number of eddies found during a season, the area of the inner-shelf subject to additional small-scale eddy fluxes due to the presence of the shoals is limited to an area not larger that the shoals itself in both seasons.

To the west, the occurrence of eddies along the western boundary is less often linked to the phase of the tide in the area, but more to the direction of the wind and the dominant along-shelf flow, suggesting that flow around the topography is important. However, the location of the eddy hot spot along the western edge changes from winter to summer, suggesting that stratification is likely to also be a factor. Inshore, where the eddies crossed the locations of multiple moorings, eddies were seen to form both within an existing horizontal density structure, such that the eddy streamlines align with near-surface isopyncals, as well as form across isopyncals and advect or deform the existing horizontal density structure. For most of the eddy types, wind direction might control the eddy formation as wind direction appears to control the larger scale flow field and its interaction with the existing bathymetric barriers. Eddies found offshore during times of good SST imagery consistently had eddy streamlines aligned with isotherms (Figure 11). If representative of the bulk of offshore eddies, this suggests that baroclinic effects and not wind or direct topographic effects might have been the dominant driver of eddy activity offshore.

5.3. The Implications of Lateral Variability on Exchange

The depth-dependent wind-driven, eddy, and background transports are each assessments of different processes that cause circulation and exchange across the inner-shelf south of Martha's Vineyard. The across-shelf surface layer transport due to winds, averaged over the mooring array (Figure 6 and Table 5), was onshore in summer but with transport magnitudes, integrated over the summer, that were similar to the volume of the inner shelf itself inshore of the 25 m isobath ($\sim 1.2 \times 10^5$ versus $\sim 1 \times 10^5$ m^3/along-shelf m). Spatial variations of the response to wind forcing seen in the depth-dependent surface layer transport as well as the relative effects of eddies were significant (Figure 6), adding 1–2 additional inner-shelf volumes of exchange each in the form of large-scale horizontal stirring. The spatial structure of the background flow (Figure 5 and Table 4) amounts to 2-2.5 inner-shelf volumes of exchange integrated over the summer season. Thus, integrated over a full season, the exchange of particles across the Martha's Vineyard inner shelf was driven predominately by lateral variability and not along-shelf uniform wind-driven dynamics. While the exact magnitude and impact of the relative exchange for wind and eddy-driven processes are difficult to determine, the background circulation that causes the large-scale relative exchange is not, and has been shown to lead to real fluxes of heat across the shelf [*Wilkin*, 2006; *Fewings and Lentz*, 2011; *Kirincich et al*., 2013].

5.4. The Consistency of Transport Estimates

It is possible that a portion of the wind-driven regression intercept seen at the moorings, which generally counterbalanced the wind-driven transport, might be the result of the larger scale effects of the eddies as illustrated above by the relative transport of an along-shelf line of particles. Coherent eddies move offshore and to the west in the area of moorings D and F, more so than at other moorings, which would potentially contribute a sizable nonwind transport at these locations (Figure 6). In contrast, at mooring B, there is little net translation of eddies, but mooring B is consistently on the northeast side of cyclonic eddies along the western edge (Figure 9) where the larger scale flow outside of the eddy is to the northwest.

That there is less variability in the regression intercept at the onshore moorings, where less eddies were observed, suggests that other processes might be driving the residual transport onshore. Here, differences between the Eulerian wave-driven return flow captured by the ADCPs and the theoretical Stokes drift vertical structure used to account for it here, or errors in the wave estimates themselves [*Fewings et al*., 2008], might be a key element of the difference. Notably, the magnitude of the residual is consistent (2000 ± 200 m^2) at onshore moorings A, C, and G, which all span the entire summer, and where the effects of the wave-driven return flow should be larger in relative magnitude. Regardless, compared to the wind-driven exchange both the lateral exchange due to coherent eddies and the large scale lateral variations in

the background (monthly mean) flow field resulted in significantly more volume exchange than what was predicted or observed due to the wind alone.

5.5. The Implications for Other Coastal Systems

While large, the background exchange was driven by tidal rectification, in contrast to the wind and a number of the characteristic eddy-driven exchange processes, and thus is not likely to be as important in other coastal systems without strong bathymetric or tidal gradients. The coherent eddies identified using the eddy-finding methodology were small in spatial scale, short-lived in time, and occurred in addition to the wind-driven transport. Thus eddies represent additional transport that has not been accounted for in typical mooring-based estimates of exchange. While many of the eddies found onshore appeared to be caused by a combination of flow-topography effects and wind directions, an important aspect of their generation was likely related to changes in the wind direction itself, a feature that is independent of the bathymetry. In contrast, the generally larger eddies found offshore represent a potentially critical source of spatially variable stirring to the inner shelf that is likely to be present in all locations. The recent modeling studies of *Brink* [2015] and *Brink and Seo* [2015] have documented that baroclinic gradients over the inner shelf and/or changing wind directions generates similar types of eddies that play a significant role in the flux of heat and momentum across the shelf.

Finally, the effects of lateral variability described here have been shown to be important relative to the strength of the depth-dependent wind-forced exchange observed on the Martha's Vineyard inner shelf. However, the magnitude of this circulation, integrated over the stratified summer season for example, is small relative to stronger upwelling regions such as the Oregon or California coast. Taking conditions typical of the Oregon coast, for example, the volume of the inner shelf is smaller and the integrated surface layer transport over the summer upwelling season is larger than Martha's Vineyard in comparison. Using values for the inner-shelf width and the observed across-shelf transport from *Kirincich et al*. [2005], the Oregon inner shelf realizes wind-driven exchange equal to 6–10 times the volume of the inner shelf over the summer upwelling season in comparison. Thus, the relative impact of lateral sources of variability on the total exchange is likely to be larger in areas of reduced or "less effective" wind forcing and/or wider inner shelves.

5.6. Missing Processes

This study has not addressed the role of lateral variability in leading to the mixing of water properties or driving the flux of quantities (i.e., heat or salt) across the inner shelf [*Wilkin*, 2006; *Fewings and Lentz*, 2011; *Kirincich et al*., 2013]. By focusing solely on the potential for volume exchange, the results described here are relevant for understanding the translation of water particles across the shelf independent of potential mixing between water particles. While difficult to constrain with the data available, the mixing of water masses during episodic wind or eddy events would increase the effective exchange above that realized via analysis of the mean (net) transport only. An important source of uncertainty is whether the mixing and exchange from depth-dependent forcings (i.e., wind-driven upwelling or downwelling) is notably different than the mixing of lateral processes, leading to a larger effect on the transfer of properties across the shelf. Additionally, eddies themselves only account for a fraction of the relative volume exchange present during an eddy due to both the definition of an eddy and the conditions that lead to eddy formation. Thus, the role of incoherent small-scale features on horizontal exchange and stirring is a critical component that is missing from this analysis.

Finally, this work does not address the potential vertical advection by the submesoscale features that comprise most of the small-scale coherent eddies found here. As shown by *Kirincich* [2016], inner-shelf eddies have measurable levels of surface convergence and divergence that suggest vertical motions of 1–3 m/d. While this is potentially small relative to areas with stronger upwelling [e.g., *Kirincich et al*., 2005], given the fluctuating wind forcing observed, it may be an important contribution. Ongoing efforts with this data set are examining the role of incoherent stirring on exchange across the inner shelf as well as the implications on the flux of heat and salt through the inner shelf.

6. Summary and Conclusions

Numerous sources of lateral variability exist over the inner-shelf south of Martha's Vineyard. Depth-dependent wind-driven across-shelf transport varied both in the magnitude and the direction of the exchange over relatively short spatial scales (10–15 km). While forcing from the across-shelf wind tended to

dominate the across-shelf wind-driven response onshore at the 15 m isobath, the response at the 25 m isobath was complicated by changes in the alignment of the principal axis of flow and potentially, the proximity to bathymetric features. Submesoscale eddies with scales generally smaller than 10 h and 6 km were frequently found over the inner shelf with vertical scales of 5–10 m. Eddies tended to occur in key areas along the south coast of Martha's Vineyard including along the western edge of the island, south and west of Wasque Shoals located to the east, and more generally offshore and removed from direct topographic influence. The occurrence of eddies was related to a combination of tidal and intermittent wind forcing effects onshore, but appears more due to buoyancy variability offshore. At slowly varying time scales of months or longer, strong spatial variability existed in the inner-shelf circulation due to the influence of the tides, bathymetry, seasonally varying winds, and stratification.

The total exchange across the inner-shelf south of Martha's Vineyard, MA was a complex combination of wind-driven depth-dependent exchange, transport due to coherent eddies, as well as the effects of a mean background circulation. Due to the short time scales of the fluctuating winds, wind forcing itself had a surprisingly small integrated effect on the along-shelf uniform across-shelf exchange, in terms of the total volume of the inner shelf "upwelled" over the summer stratified period. Components of the depth-dependent exchange across the inner shelf were generally consistent with wind-driven theory, yet the total observed transport often opposed the wind-driven exchange. The integrated effect of small-scale lateral variations suggests that lateral exchange due to coherent eddies can make an important contribution to volume transport across the inner shelf near areas of complex topography or more variable wind conditions.

Appendix A: Surface Current Data Quality

The quality of the surface current observations were assessed in multiple ways. First, comparisons were made between the velocity in the surface-most bin of the ADCPs (at 2–4 m depth) and the nearest spatial average of the HF radar velocity, measuring the top 0.5 m [*Stewart and Joy*, 1974]. While real differences exist between the two measurement types due to the separation distance and spatial extent [*Graber et al*., 1997; *Shay et al*., 2007], ADCP to HF radar comparisons are often used to identify whether significant differences between these observations exist that might be due to instrumental noise or bias [see review by *Paduan and Washburn*, 2013]. For the 30 min averaged east velocity component, these comparisons, as rms differences range from 6 to 10 cm s^{-1}. RMS differences were generally smaller inshore and to the west, with moorings C and B having the smallest differences, while F and I had largest differences, driven in part by the strong spatial variability in tidal velocities that existed along the eastern edge of the study area [*Kirincich et al*., 2013].

Second, two mass drifter releases within the study period were used by *Rypina et al*. [2016] to make both Eulerian and Lagrangian comparisons between the drifter velocities and trajectories and that possible from the HF radar results. Eulerian comparisons between the drifter velocities and radar velocities had mean bias of 1-4 cm s^{-1} and std dev of 4–7 cm s^{-1}. Lagrangian comparisons between the drifter trajectories and pseudotrajectories launched within the HF radar field had mean separation speeds of 2.5-5 cm s^{-1}. Importantly, these results varied systematically between the releases with the release during stronger wind forcing having smaller differences, likely due to environmental conditions favoring larger spatial scales of variability that were better resolved by the radar [*Rypina et al*., 2014, 2016].

Acknowledgments
The 2014 ISLE field study as well as this analysis was supported by NSF OCE grant 1332646 and the Woods Hole Oceanographic Institution. The authors also thank Craig Marquette for his tireless efforts preparing, deploying, and recovering all of the moored instrumentation as well as Irina Rypina and Ken Brink for their helpful comments and insight. The raw data used in this study are available at the WHOI data library archive (DOI:10.1575/1912/8740).

References

Allen, J. (1980), Models of wind-driven currents on the continental shelf, *Annu. Rev. Fluid Mech.*, *12*, 389–433.
Austin, J. A., and S. J. Lentz (2002), The inner shelf response to wind-driven upwelling and downwelling, *J. Phys. Oceanogr.*, *32*, 2171.
Barrick, D. E. (2002), Geometrical dilution of statistical accuracy (GDOSA) in multi-static HF radar networks, CODAR Ocean Sensors, Mountain View, Calif. [Available at http://www.codaros.com/Manuals/SeaSonde/Docs/Informative/GDOSA_Definition.pdf.]
Brink, K. H. (2015), Continental shelf baroclinic instability 1: Relaxation from upwelling or downwelling, *J. Phys. Oceanogr.*, *46*, 551–568, doi: 10.1175/JPO-D-15-0047.1.
Brink, K. H., and H. Seo (2015), Continental shelf baroclinic instability 2: Oscillating wind forcing, *J. Phys. Oceanogr.*, *46*, 569–582, doi: 10.1175/JPO-D-15-0048.1.
Capet, X., J. C. McWilliams, M. J. Molemaker, and A. F. Shchepetkin (2008), Mesoscale to submesoscale transition in the California Current System. Part I: Flow structure, eddy flux, and observational tests, *J. Phys. Oceanogr.*, *38*(1), 29–43, doi:10.1175/2007JPO3671.1.
Castelao, R. M., and J. A. Barth (2006), The relative importance of wind strength and along-shelf bathymetric variations on the separation of a coastal upwelling jet, *J. Phys. Oceanogr.*, *36*, 412–425.
Chelton, D. B., M. G. Schlax, and R. M. Samelson (2011), Global observations of nonlinear mesoscale eddies, *Prog. Oceanogr.*, *91*(2), 167–216, doi:10.1016/j.pocean.2011.01.002.

Dudas, S. E., B. A. Grantham, A. R. Kirincich, B. A. Menge, J. Lubchenco, and J. A. Barth (2009), Current reversals as determinants of intertidal recruitment on the central Oregon coast, *ICES J. Mar. Sci.*, *66*, 396–407, doi:10.1093/icesjms/fsn179.

Fairall, C. W., E. F. Bradley, J. E. Hare, A. A. Grachev, and J. B. Edson (2003), Bulk parameterizations of air-sea fluxes: Updates and verification for the COARE algorithm, *J. Clim.*, *16*, 571–591.

Fewings, M., and S. J. Lentz (2011), Summertime cooling of the shallow continental shelf, *J. Geophys. Res.*, *116*, C07015, doi:10.1029/2010JC006744.

Fewings, M., S. J. Lentz, and J. Fredericks (2008), Observations of cross-shelf flow driven by cross-shelf winds on the inner continental shelf, *J. Phys. Oceanogr.*, *38*, 2358–2378, doi:10.1175/2008JPO3990.1.

Ganju, N. K., S. J. Lentz, A. R. Kirincich, and J. T. Farrar (2011), Complex mean circulation over the inner-shelf south of Martha's Vineyard revealed by observations and a high-resolution model, *J. Geophys. Res.*, *116*, C10036, doi:10.1029/2011JC007035.

Gordon, R. L. (1996), *Acoustic Doppler Current Profiler: Principles of Operation, a Practical Primer Second edition for Broadband ADCPs*, 54 pp., RDI Instrum., San Diego, Calif.

Graber, H. C., B. K. Haus, R. D. Chapman, and L. K. Shay (1997), HF radar comparisons with moored estimates of current speed and direction: Expected differences and implications, *J. Geophys. Res.*, *102*(C8), 18,749–18,766.

Horwitz, R., and S. J. Lentz (2014), Inner-shelf response to cross-shelf wind stress: The importance of the cross-shelf density gradient in an idealized numerical model and field observations, *J. Phys. Oceanogr.*, *44*(2008), 86–103, doi:10.1175/JPO-D-13-075.1.

Huyer, A. (1990), Shelf circulation, in *Sea*, vol. 9a, chap. 12, edited by B. LeMehaute and D. M. Hanes, pp. 1647–1658, John Wiley, New York.

Huyer, A., J. H. Fleischbein, J. Keister, P. M. Kosro, N. Perlin, R. L. Smith, and P. A. Wheeler (2005), Two coastal upwelling domains in the northern California Current system, *J. Mar. Res.*, *63*(5), 901–929, doi:10.1357/002224005774464238.

Kaplan, D. M., and J. Largier (2006), HF radar-derived origin and destination of surface waters off Bodega Bay, California, *Deep Sea Res., Part II*, *53*(25–26), 2906–2930, doi:10.1016/j.dsr2.2006.07.012.

Kim, S. Y. (2010), Observations of submesoscale eddies using high-frequency radar-derived kinematic and dynamic quantities, *Cont. Shelf Res.*, *30*(15), 1639–1655, doi:10.1016/j.csr.2010. 06.011.

Kirincich, A. (2016), The occurrence, drivers, and implications of submesoscale eddies on the Martha's Vineyard inner shelf, *J. Phys. Oceanogr.*, *46*, 2645–2662, doi:10.1175/JPO-D-15-0191.1.

Kirincich, A., and J. Barth (2009a), Alongshelf variability of inner-shelf circulation along the central Oregon coast during summer, *J. Phys. Oceanogr.*, *39*(6), 1380–1398, doi:10.1175/2008JPO3760.1.

Kirincich, A. R., and J. A. Barth (2009b), Time-varying across-shelf Ekman transport and vertical eddy viscosity on the inner shelf, *J. Phys. Oceanogr.*, *39*(3), 602–620, doi:10.1175/2008JPO3969. 1.

Kirincich, A. R., J. A. Barth, B. A. Grantham, B. A. Menge, and J. Lubchenco (2005), Wind-driven inner-shelf circulation off central Oregon during summer, *J. Geophys. Res.*, *110*, C10S03, doi:10.1029/2004JC002611.

Kirincich, A. R., T. de Paolo, and E. Terrill (2012), Improving HF radar estimates of surface currents using signal quality metrics, with application to the MVCO high-resolution radar system, *J. Atmos. Oceanic Technol.*, *29*(9), 1377–1390, doi:10.1175/JTECH-D-11-00160.1.

Kirincich, A. R., S. J. Lentz, J. T. Farrar, and N. K. Ganju (2013), The spatial structure of tidal and mean circulation over the inner shelf south of Martha's Vineyard, Massachusetts, *J. Phys. Oceanogr.*, *43*(9), 1940–1958, doi:10.1175/JPO-D-13-020.1.

Kuebel Cervantes, B. T., J. S. Allen, and R. M. Samelson (2003), A modeling study of Eulerian and Lagrangian aspects of shelf circulation off Duck, North Carolina, *J. Phys. Oceanogr.*, *33*(10), 2070–2092.

Kundu, P. K., and J. S. Allen (1976), Some three-dimensional characteristics of low-frequency current fluctuations near the Oregon Coast, *J. Phys. Oceanogr.*, *6*(2), 181–199.

Lentz, S., R. T. Guza, S. Elgar, F. Feddersen, and T. H. C. Herbers (1999), Momentum balances on the North Carolina inner shelf, *J. Geophys. Res.*, *104*(C8), 18,205–18,226.

Lentz, S. J. (1994), Current dynamics over the Northern California inner shelf, *J. Phys. Oceanogr.*, *24*, 2461–2478.

Lentz, S. J. (1995), Sensitivity of the inner-shelf circulation to the form of the eddy viscosity profile, *J. Phys. Oceanogr.*, *25*, 19–28.

Lentz, S. J. (2001), The influence of stratification on the wind-driven cross-shelf circulation over the North Carolina Shelf*, *J. Phys. Oceanogr.*, *31*(9), 2749–2760, doi:10.1175/1520-0485(2001) 031.

Lentz, S. J., and M. R. Fewings (2012), The wind- and wave-driven inner-shelf circulation, *Annu. Rev. Mar. Sci.*, *4*, 317–43, doi:10.1146/annurev-marine-120709-142745.

Lentz, S. J., and C. D. Winant (1986), Subinertial currents on the southern California shelf, *J. Phys. Oceanogr.*, *16*, 1737–1750.

Lentz, S. J., M. Fewings, P. Howd, J. Fredericks, and K. Hathaway (2008), Observations and a model of undertow over the inner continental shelf., *J. Phys. Oceanogr.*, *38*, 2341–2357.

McGillicuddy, D. J., D. M. Anderson, D. R. Lynch, and D. W. Townsend (2005), Mechanisms regulating large-scale seasonal fluctuations in Alexandrium Fundyense populations in the Gulf of Maine: Results from a physical-biological model, *Deep Sea Res., Part II*, *52*, 2698–2714, doi:10.1016/j.dsr2.2005.06.021.

Menge, B. A., et al. (2003), Coastal oceanography sets the pace of rocky intertidal community dynamics., *Proc. Natl. Acad. Sci. U. S. A.*, *100*(21), 12,229–12,234, doi:10.1073/pnas.1534875100.

Mitchum, G. T., and A. J. Clarke (1986), The frictional nearshore response to forcing by synoptic scale winds, *J. Phys. Oceanogr.*, *16*, 934–946.

Paduan, J. D., and L. Washburn (2013), High-frequency radar observations of ocean surface currents, *Annu. Rev. Mar. Sci.*, *5*, 115–36, doi:10.1146/annurev-marine-121211-172315.

Pawlowicz, R., B. Beardsley, and S. Lentz (2002), Classical tidal harmonic analysis including error estimates in MATLAB using T_TIDE, *Comput. Geosci.*, *28*(8), 929–937.

Robinson, I. (1981), Tidal vorticity and residual circulation, *Deep Sea Res., Part A*, *28*(3), 195–212.

Rypina, I., A. Kirincich, S. Lentz, and M. Sundermeyer (2016), Investigating the eddy diffusivity concept in the coastal ocean, *J. Phys. Oceanogr.*, *46*, 2201–2218.

Rypina, I. I., A. R. Kirincich, R. Limeburner, and I. A. Udovydchenkov (2014), Eulerian and Lagrangian correspondence of high-frequency radar and surface drifter data: Effects of radar resolution and flow components, *J. Atmos. Oceanic Technol.*, *31*(4), 945–966, doi:10.1175/JTECH-D-13-00146.1.

Shay, L. K., J. Martinez-Pedraja, T. M. Cook, B. K. Haus, and R. H. Weisberg (2007), High-frequency radar mapping of surface currents using WERA, *J. Atmos. Oceanic Technol.*, *24*(3), 484–503, doi:10.1175/JTECH1985.1.

Song, Y. T., D. B. Haidvogel, and S. M. Glenn (2001), Effects of topographic variability on the formation of upwelling centers off New Jersey: A theoretical model, *J. Geophys. Res.*, *106*(C5), 9223–9240.

Stewart, R. H., and J. W. Joy (1974), HF radio measurements of surface currents, *Deep Sea Res. Oceanogr. Abstr.*, *21*, 1039–1049.

Terray, E., R. Gordon, and B. Brumley (1997), Measuring wave height and direction using upward-looking ADCPs, in *Oceans MTS/IEEE Conference Proceedings*, vol. 1, pp. 287–290, IEEE, New York.

Tilburg, C. E. (2003), Across-shelf transport on a continental shelf: Do across-shelf winds matter?, *J. Phys. Oceanogr.*, *33*, 2675–2688.

Tilburg, C. E., and R. Garvine (2003), Three-dimensional flow in a shallow coastal upwelling zone: Alongshore convergence and divergence on the New Jersey shelf, *J. Phys. Oceanogr.*, *33*, 2113–2125.

Wilkin, J. (2006), The summertime heat budget and circulation of southeast New England shelf waters, *J. Phys. Oceanogr.*, *36*, 1997–2011.

Yankovsky, A. E., and D. C. Chapman (1995), Generation of mesoscale flows over the shelf and slope by shelf wave scattering in the presence of a stable, sheared mean current, *J. Geophys. Res.*, *100*(C4), 6725–6742.